Spinless electric toroidal multipoles in ferroaxial $K_2Zr(PO_4)_2$ revealed by symmetry-adapted closest Wannier analysis

Yu Xie, Rikuto Oiwa, and Satoru Hayami
Graduate School of Science, Hokkaido University, Sapporo 060-0810, Japan
(Dated: April 23, 2026)

From a symmetry perspective, ferroaxial order belongs to the same symmetry as time-reversal-even pseudovectors. Experimentally, $K_2Zr(PO_4)_2$ is known to undergo a displacive-type phase transition from a non-ferroaxial to a ferroaxial phase. To identify the key microscopic ingredients driving this transition, we carry out a quantitative analysis combining density-functional theory calculations and symmetry-adapted closest Wannier analysis. As a result, we show that electric toroidal dipole, electric toroidal octupole, and electric hexadecapole, which belong to the same irreducible representation, make dominant contributions to the ferroaxial transition. In particular, we find that spinless electric toroidal octupoles, which originate from spin-independent off-diagonal real hopping between the p orbitals on P and O atoms and between the d orbitals on Zr atoms and p orbitals on O atoms, provide the most significant contributions. Moreover, we explicitly analyze the orbital characters involved in the relevant hybridizations associated with these multipoles. We further show that the relativistic spin–orbit coupling has a negligible influence on the ferroaxial transition. These results demonstrate that spin-independent orbital hybridization between different orbitals on different atoms plays a crucial role in inducing the ferroaxial transition.

I. INTRODUCTION

Ferroaxiality arises from the breaking of certain mirror symmetries while preserving both time-reversal ($\mathcal{T}$) and spatial-inversion ($\mathcal{P}$) symmetries [1]. Such space-time inversion properties stand in sharp contrast to those of ferromagnetism, which breaks $\mathcal{T}$ symmetry, and ferroelectricity, which breaks $\mathcal{P}$ symmetry [2, 3]. In this sense, ferroaxiality is neither magnetic nor electric in nature, and at first glance, it may appear to be a rather featureless state.

The experimental identification of ferroaxial transition in $RbFe(MoO_4)_2$ has opened up an avenue of research [1, 4–6]. Indeed, ferroaxial order has since been discovered in the materials $NiTiO_3$ [7–10], $Ca_5Ir_3O_{12}$ [11–14], $BaCoSiO_4$ [15], $Na_2Hf(BO_3)_2$ [16], Na-superionic conductors [17], $MnTiO_3$ [18], and $EuTe_3$ [19]. In parallel, theoretical studies have uncovered two characteristic classes of physical phenomena associated with ferroaxial ordering: The first involves off-diagonal responses of conjugated physical quantities, including antisymmetric thermopolarization [20], longitudinal spin current generation [21, 22], and nonlinear transverse magnetization [23, 24]; The second concerns cross correlations between chiral and polar degrees of freedom [25–27], exemplified by the electrogyration effect [7, 28] and surface-induced chiral-domain selection [29].

In many ferroaxial materials, the ferroaxial transition is characterized as a structural transition accompanied by rotational atomic displacements. However, studies of how such structural transitions affect the electronic degrees of freedom have been largely limited to model calculations [30], and quantitative analyses have been scarce [31]. Moreover, although several microscopic mechanisms have been proposed for the electric toroidal dipole (ETD)—the order parameter of ferroaxial order—such as vortices of electric polarization [Fig. 1(a)] [32, 33] and cross-product–type spin–orbit coupling (SOC) $\boldsymbol{l} \times \boldsymbol{\sigma}$ [34], where $\boldsymbol{l}$ and $\boldsymbol{\sigma}$ denote the orbital and spin angular momenta, their relative importance in real materials remains unclear. Furthermore, recent studies have shown that cluster-type orbital ordering also leads to a net ferroaxial moment corresponding to ETD [Fig. 1(a)] [14], as well as an antiferro-type ferroaxial moment corresponding to an electric toroidal quadrupole (ETQ) [Fig. 1(b)] [35, 36]. Consequently, it is still unknown which electronic degrees of freedom play the primary role in characterizing ferroaxial order. These issues highlight the necessity of theoretical analyses that start from realistic electronic structures in materials.

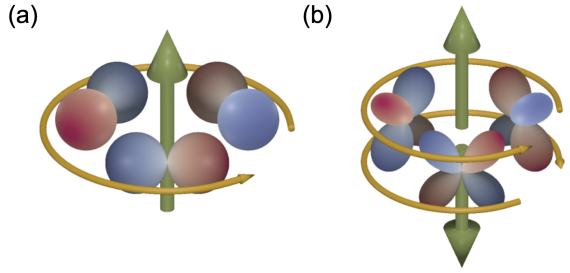

FIG. 1: Schematic illustration of the intuitive images of (a) ETD and (b) ETQ moments under cluster-type orbital orderings. Red and blue indicate positive and negative phases, respectively, and green arrows denote the ETD.

Motivated by these considerations, we investigate the prototypical ferroaxial material, $K_2Zr(PO_4)_2$, which undergoes a displacive-type ferroaxial transition at approximately 700 K [37]. In this transition, the crystal symmetry changes from the nonferroaxial structure $P\bar{3}m1$

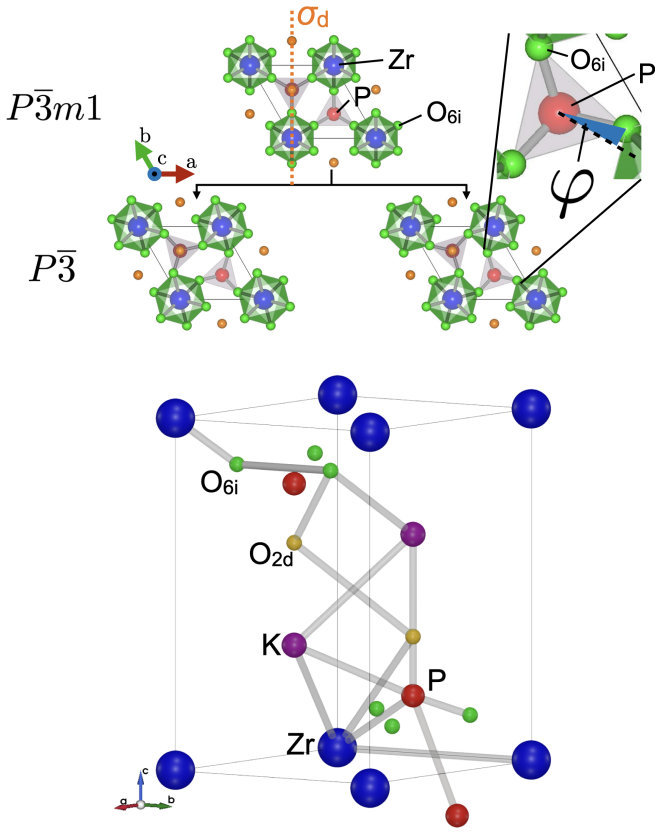

FIG. 2: (a) Crystal structure of $K_2Zr(PO_4)_2$ in the non-ferroaxial phase ($P\bar{3}m1$, top) and the ferroaxial phase ($P\bar{3}$, bottom). Atoms in blue, red, green, and orange correspond to Zr, P, O_{6i}, and O_{2d} atoms, respectively, while K atoms are positioned underneath the P and O_{2d}. Here, O_{6i} and O_{2d} denote the O atoms at the 6i and 2d Wyckoff positions in $P\bar{3}m1$. The rotation angle φ of the PO_4 tetrahedra characterizes the degree of ferroaxiality. (b) Nearest-neighbor ($n = 1$) bonds in Eq. (6), defined by the shortest interatomic distances.

(#164, D^1_{3d}) to the ferroaxial structure $P\bar{3}$ (#147, C^1_{3i}), as illustrated in Fig. 2(a). According to the rotation of the PO_4 tetrahedra (or ZrO_6 octahedra) by the rotation angle φ, the vertical mirror symmetry σ_d is broken while retaining threefold rotational symmetry. Since φ takes a finite value only in the $P\bar{3}$ phase, it serves as a quantitative measure of ferroaxiality from the viewpoint of the lattice degree of freedom. In this situation, it is expected that corresponding electronic ferroaxial degrees of freedom also become nonzero. For example, it has been confirmed for the cross–product–type SOC defined at the P site [31], whereas systematic quantitative comparisons among the various ferroaxial electronic degrees of freedom, including spinless degrees of freedom, have not yet been performed.

In the present study, we perform a detailed quantitative analysis of the ferroaxial compound $K_2Zr(PO_4)_2$ to clarify the role of the microscopic electronic degrees of freedom under a static rotational distortion. Employing density-functional theory (DFT) calculations in combination with a symmetry-adapted closest Wannier (SymCW) method [38, 39], we examine how the ferroaxial-related electronic degrees of freedom evolve as a function of the rotation angle. Within a complete multipole operator basis set, we find that various multipolar degrees of freedom, such as the ETD, electric toroidal octupole (ETO), and electric hexadecapole (EH), emerge as multi-site spinless bases that significantly affect the electronic structure. Especially, we demonstrate that the two ETOs, expressed in terms of hybridizations between the p orbitals on P atoms and d orbitals on Zr atoms and between the p orbitals on P and O atoms, provide the dominant contributions to the ferroaxial transition. We further show that relativistic SOC has only a negligible influence on the ferroaxial transition.

The remainder of this paper is organized as follows. In Sec. II, we show the electronic degrees of freedom related to ferroaxiality in the displacive-type ferroaxial transition of $K_2Zr(PO_4)_2$, based on the symmetry-adapted multipole framework. Section III presents the electronic band structures and orbital-resolved density of states obtained by the DFT calculations. Section IV provides the effective tight-binding model derived from the DFT calculations using the SymCW method. Section V presents a multipole-based classification of ferroaxial degrees of freedom, which allows us to identify the essential electronic degrees of freedom arising from the entanglement of orbital and bond. We also present the dominant multipole contributions that emerge when the ferroaxial order occurs. Finally, Sec. VI summarizes our findings and presents the perspective for future studies.

II. FERROAXIAL DEGREES OF FREEDOM BASED ON MULTIPOLE REPRESENTATION

Ferroaxial degrees of freedom can be described unambiguously within the framework of the symmetry-adapted multipole operator basis (SAMB), which has been established recently [40]. SAMBs consist of four types of multipoles, which are classified as electric (E: Q), magnetic (M: M), magnetic toroidal (MT: T), and electric toroidal (ET: G) multipoles according to their $\mathcal{P}$ and $\mathcal{T}$ parities [34, 41, 42]. For a given symmetry group, each multipole $X^{\Gamma}_{l\gamma}$ ($X = Q, M, T, G$) is further characterized by its rank l, the irreducible representation (IR) Γ, and its component γ. Since the SAMB constitutes a complete operator basis set in a given physical space, any degrees of freedom, such as orbital, spin, bond, and their composites, can be described in a unified way.

For later convenience, we show the representative electronic ferroaxial degrees of freedom in $K_2Zr(PO_4)_2$. We here consider the unit consisting of upward and downward triangles connected by the spatial inversion symmetry in Fig. 3, which corresponds to the PO_4 tetrahe-

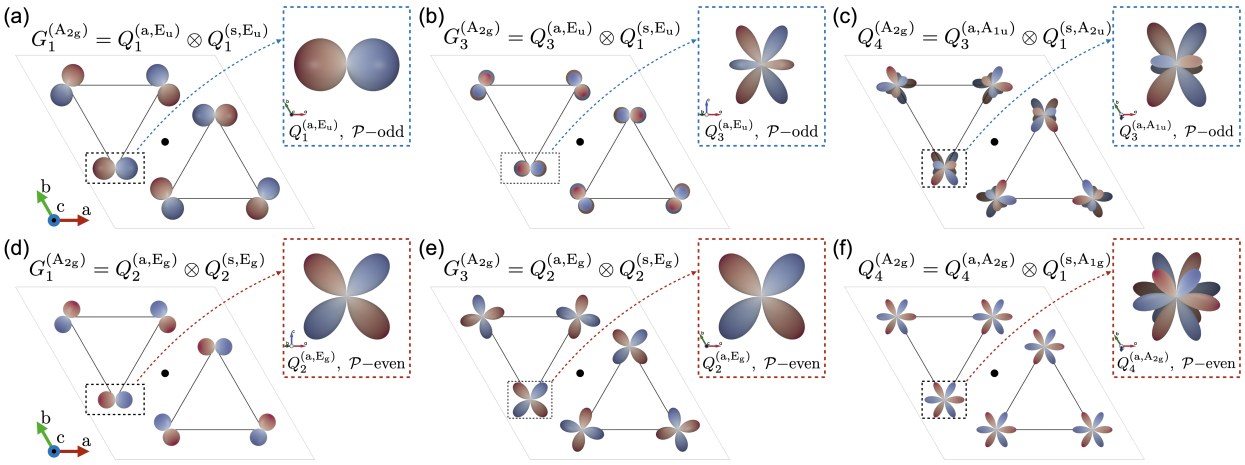

FIG. 3: Examples of SAMBs belonging to the A_{2g} irreducible representation (IR) of the D_{3d} point group in a six-site cluster. The resulting A_{2g} multipoles are (a, d) the ETD, (b, e) the ETO, and (c,f) the EH. The atomic SAMBs are $\mathcal{P}$-odd in (a)–(c) and $\mathcal{P}$-even in (d)–(f). All the SAMBs retain the spatial inversion symmetry in terms of the inversion center denoted by the black dots.

TABLE I: Correspondence between the atomic orbital hybridization and the atomic SAMBs in $K_2Zr(PO_4)_2$ without the spin degree of freedom. The subscript associated with a multipole $X = Q, M, T, G$ specifies its rank.

Orbital	Atomic SAMBs	
	$\mathcal{P}$-even	$\mathcal{P}$-odd
s-*s*	Q_0	-
s-*p*	-	Q_1, T_1
s-*d*	Q_2, T_2	-
p-*p*	Q_0, Q_2, M_1	-
p-*d*	-	Q_1, Q_3, G_2, T_1, T_3, M_2
d-*d*	Q_0, Q_2, Q_4, M_1, M_3	-

dra in Fig. 2(a). Since the ferroaxial degree of freedom corresponds to the A_{2g} IR in the high-temperature non-ferroaxial phase under the symmetry $P\bar{3}m1$, we show how to construct the electronic ferroaxial degrees of freedom belonging to the A_{2g} IR based on the SAMB.

The SAMB is constructed by the product of the atomic degrees of freedom and the site/bond degrees of freedom; the former is referred to as the atomic SAMB (denoted by $Y_l^{(a,\Gamma)}$) [43] and the latter is referred to as the cluster SAMB (denoted by $Y_l^{(s,\Gamma)}$ for site and $Y_l^{(b,\Gamma)}$ for bond) for $Y = Q, M, T, G$ [44, 45]. The atomic SAMBs relevant to $K_2Zr(PO_4)_2$, spanning the *s*-, *p*-, and *d*-orbital manifolds, are summarized in Table I, where the $\mathcal{P}$-even multipoles (Q_0, Q_2, Q_4, M_1, M_3, and T_2) are activated in the orbital space with even-parity hybridization, while the $\mathcal{P}$-odd multipoles (Q_1, Q_3, G_2, M_2, T_1, and T_3) are activated in the orbital space with odd-parity hybridization. The cluster SAMBs relevant to $K_2Zr(PO_4)_2$ can be obtained in an analogous manner by incorporating the permutation symmetries among the sites [40].

Since the A_{2g} representation can be constructed from the direct products $A_{1g} \otimes A_{2g}$, $A_{1u} \otimes A_{2u}$, $E_g \otimes E_g$, and $E_u \otimes E_u$, the SAMBs corresponding to the ferroaxial degree of freedom are obtained by appropriately combining atomic and cluster SAMBs in a way that preserves the symmetry. We show several specific examples in the case of the site-cluster SAMB in Fig. 3. The ferroaxial degrees of freedom can be constructed by arranging the atomic electric dipole [Fig. 3(a)] and two different electric octupoles [Figs. 3(b) and 3(c)], two different electric quadrupoles [Figs. 3(d) and 3(e)], and electric hexadecaple [Fig. 3(f)] so as to satisfy spatial inversion and threefold rotational symmetries. By taking into account the rank of multipoles, the ferroaxial degrees of freedom in Figs. 3(a)–3(f) are identified as two ETDs [Figs. 3(a) and 3(d)], two ETOs [Figs. 3(b) and 3(e)], and two EHs [Figs. 3(c) and 3(f)]. Similarly, one can construct the ferroaxial degrees of freedom by the product of atomic and bond-cluster SAMBs by considering the bond degree of freedom instead of the site one.

III. DFT CALCULATIONS

We calculate the electronic states of $K_2Zr(PO_4)_2$ based on DFT calculations by using Quantum ESPRESSO [46]. In the following calculations, we adopt the PBE exchange-correlation functional and use the scalar relativistic optimized norm-conserving Vanderbilt (ONCV) pseudopotentials [47] downloaded from PseudoDojo [48].

We first use the experimental lattice constants $a = 5.3233$ Å and $c = 8.8361$ Å for the non-ferroaxial phase with the rotation angle $\varphi = 0°$ [37]. Then, by performing a structural optimization of the lattice constants and atomic positions, we obtain the optimized lattice constants $a = 5.2759$ Å and $c = 9.0651$ Å, and the atomic rotation angle $\varphi = \pm 16.89°$, which is consistent with the experimental value of $\varphi \sim 17°$ in the ferroaxial phase at 300 K [37]. Here the positive (negative) sign of φ is defined as counterclockwise (clockwise) rotations of the PO_4 tetrahedra.

Then, we perform self-consistent DFT calculations for $\pm 16.89°$ and $\varphi = 0°$. The kinetic-energy cutoff for the Kohn–Sham (KS) orbitals and the total–energy convergence threshold are set to 100 Ry and 1×10^{-14} Ry, respectively. The $\boldsymbol{k}$-point grid is set to $12 \times 12 \times 6$. The obtained band structures and partial (orbital-resolved) density of states (DOS) for $\varphi = \pm 16.89°$ and $0°$ are shown in Figs. 4(a) and (b), respectively. According to the DOS analysis, the s and p orbitals of P and O_{6i}, and the d orbitals of Zr contribute predominantly to the electronic states around -20 eV $\lesssim E \lesssim 7$ eV, including the Fermi level, which is set to 0 eV. In contrast, the s and p orbitals of Zr make negligible contributions near the Fermi level. The contributions of the $4s$ and $3p$ orbitals of K, as well as the $2s$ and $2p$ orbitals of O_{2d} are also finite, which are not shown in Fig. 4. Here and hereafter, we denote two O atoms at the 6i and 2d Wyckoff positions in $P\bar{3}m1$ as O_{6i} and O_{2d}.

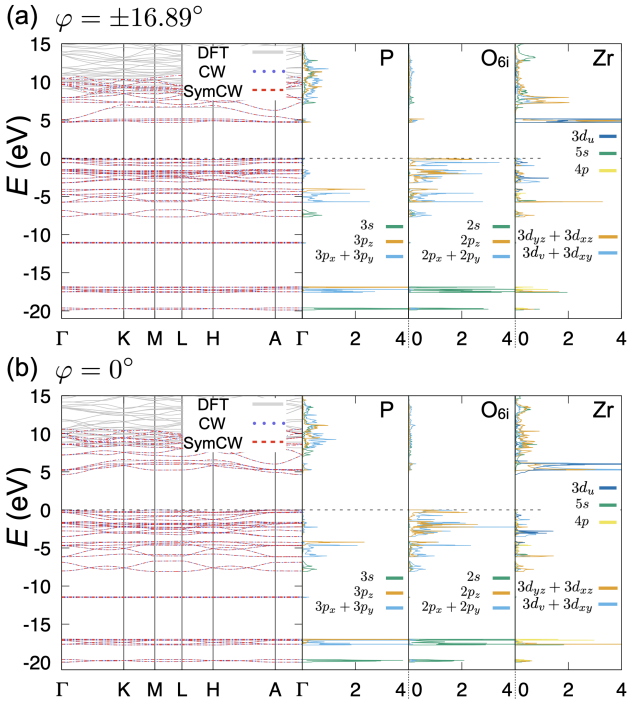

FIG. 4: Band structures and densities of states (DOS) obtained from DFT calculations, together with the fitting results of the CW and SymCW models. Panels (a) and (b) correspond to rotation angles of $\varphi = \pm 16.89°$ and $\varphi = 0°$, respectively. In the left panel, gray lines represent the DFT bands, while red and blue lines show the band structures obtained by the CW and SymCW models. The DOS per atom for orbitals of P, O_{6i}, and Zr are shown in the right panel; the in-plane (xy) and $d_u \equiv d_{3z^2-r^2}$ components are represented in blue, the out-of-plane component in orange, the s orbital in green, and the $4p$ orbital in yellow. The proposed models reproduce the DFT results well up to about 7 eV above the Fermi level, which is the energy range relevant to most physical properties.

IV. SYMMETRY-ADAPTED CLOSEST WANNIER MODEL

In this section, we construct the symmetry-adapted closest Wannier model for $K_2Zr(PO_4)_2$ by using the SymCW method, implemented in the open-source Python library SymClosestWannier [38, 39].

For the initial guess of the closest Wannier functions (CWFs), we use the hydrogenic atomic s and p orbitals for P, K, O_{6i}, O_{2d} and d orbitals for Zr, where the total number of orbitals is 53 in the unit cell. The s and p orbitals of Zr are omitted from the model because their contributions are negligible. The upper and lower energy windows $(\mu_{\max}, \mu_{\min})$ and the corresponding smearing temperatures $(\sigma_{\max}, \sigma_{\min})$, used for the CW method [38], are set to $(\mu_{\max}, \mu_{\min}) = (4.8 \text{ eV}, -23 \text{ eV})$ and $(\sigma_{\max}, \sigma_{\min}) = (1 \text{ eV}, 0 \text{ eV})$, respectively. These parameters are chosen so that the CW Hamiltonian reproduces the DFT band dispersion with high accuracy while keeping the spread of the CWFs sufficiently small. We have also confirmed that the results and physical interpretations remain unchanged within a reasonable range of the energy windows and smearing temperatures. Therefore, the conclusions obtained from the SymCW model are robust against such parameter choices. Note that the symmetry properties of the CWFs are inherited from those of the original atomic orbitals used as the initial guess [38, 39]. Therefore, SAMBs, a complete orthonormal operator basis set $\{\mathbb{Z}_j\}$, can be defined for the CWF space. Using this operator basis, the 53×53 closest Wannier (CW) tight-binding Hamiltonian, H^{CW}, can be expressed as a linear combination of $\{\mathbb{Z}_j\}$ as

$$H^{\mathrm{SymCW}} = \sum_{j}^{\Gamma_j \in \mathrm{A_{1g}},\, \mathrm{A_{2g}}} z_j \mathbb{Z}_j, \tag{1}$$

$$z_j = \mathrm{Tr}\left(\mathbb{Z}_j H^{\mathrm{CW}}\right), \tag{2}$$

where z_j is the corresponding weight of each SAMB $\mathbb{Z}_j$ with the unit of energy (eV). Here, we ignore the spin degree of freedom, whose effect will be discussed in Sec. V C. We refer to this symmetrized model as the SymCW model. The SAMBs $\{\mathbb{Z}_j\}$, belonging to the A_{1g} and A_{2g} IRs of the D_{3d} point group, are automatically generated using the open-source Python library Multi-

Pie [40]. The total number of SAMBs is 96,439, by considering up to the 200 bond-clusters for each bond (the maximum bond length is about the distance between the home unit-cell and the 10th neighbor unit-cell).

[The band energy has been removed because it is not discussed in the main text, and the expectation value has been moved to a more appropriate place.]

The mean absolute error between the energy eigenvalues obtained from the DFT calculations and the SymCW models under the Fermi level is evaluated as

$$\eta = \sum_{\boldsymbol{k}} \sum_{n=1}^{N_{\rm F}} \frac{\left|\epsilon_{n\boldsymbol{k}}^{\rm DFT} - \epsilon_{n\boldsymbol{k}}^{\rm SymCW}\right|}{N_k N_{\rm F}} = \begin{cases} 0.02667 \text{ meV} \\ \qquad (\varphi = \pm 16.89^\circ), \\ 0.02238 \text{ meV} \\ \qquad (\varphi = 0^\circ), \end{cases} \tag{3}$$

where $N_{\rm F}$ denotes the number of eigenvalues below the Fermi level and $N_k = 864$ ($12\times12\times6$) is the number of $\boldsymbol{k}$ points used in the DFT calculations. As shown in Fig. 4, the CW and SymCW models accurately reproduce the valence band structure of DFT calculations for both the $P\bar{3}$ ($\varphi = \pm 16.89^\circ$) and $P\bar{3}m1$ ($\varphi = 0^\circ$) phases. Although the conduction bands above 7 eV, particularly those near the K and H points, are not well reproduced, this inaccuracy does not affect the results discussed below.

V. RESULTS AND DISCUSSIONS

In this section, we present an analysis on the spinless electric toroidal multipoles in the ferroaxial phase of $K_2Zr(PO_4)_2$, which affects the electronic structure. We first show the explicit definitions of several SAMBs together with their physical interpretations, highlighting their roles as key microscopic ingredients of the ferroaxial order. We then present the evolution of their expectation value of each SAMB with varying the rotation angle φ and identify the dominant contributions to the ferroaxial transition.

A. Microscopic representation of ferroaxial mutlipoles

Let us first show the microscopic representation of the SAMBs describing the ferroaxial order and analyze our models for the $P\bar{3}$ ($\varphi = \pm 16.89^\circ$) and $P\bar{3}m1$ ($\varphi = 0^\circ$) structures. The SymCW Hamiltonian in Eq. (1) can be rewritten as

$$H^{\rm SymCW} = H_{\rm CEF} + H_{\rm hop}, \tag{4}$$

$$H_{\rm CEF} = H_{\rm CEF}^{\rm (K)} + H_{\rm CEF}^{\rm (Zr)} + H_{\rm CEF}^{\rm (P)} + H_{\rm CEF}^{\rm (O_{6i})} + H_{\rm CEF}^{\rm (O_{2d})}, \tag{5}$$

$$H_{\rm hop} = \sum_{n=1}^{200} \sum_{\langle M,N\rangle}^{\rm Zr,K,P,O_{6i},O_{2d}} H_{\rm hop}^{(M-N,n)}, \tag{6}$$

where $H_{\rm CEF}^{(M)}$ is the crystalline electric field (CEF) term at M = K, Zr, P, O_{6i}, O_{2d} atoms and $H_{\rm hop}^{(M-N,n)}$ represents the spin-independent hopping term in the n-th bond-cluster of the M–N bond between M and N atoms. The explicit definition of the nearest-neighbor ($n = 1$) bonds are shown in Fig. 2(b).

Each term is expressed as the linear combination of SAMBs $\{\mathbb{Z}_j\}$, and their coefficients $\{z_j\}$ can be obtained by computing Eq. (2). We consider 96,439 SAMBs by including up to the 200 bond-clusters for each bond. Among these SAMBs, 14121 is the number of multipoles belonging to the A_{2g} IR of the D_{3d} point group symmetry. Especially, we hereafter focus on the representative ferroaxial SAMBs including ETD G_z, ETOs G_{3b} and $G_{z\alpha}$, and EH Q_{4b}, whose coefficients are significantly large. As for the hopping terms, we restrict our analysis to the nearest-neighbor term $H_{\rm hop}^{(M-N,1)}$, since we have confirmed that the further-neighbor hoppings are negligibly small, with their magnitudes decaying exponentially beyond the second-nearest neighbors.

The explicit definitions of these SAMBs, together with their coefficients and expectation values at $\varphi = \pm 16.89^\circ$, 0°, are summarized in Table II. In order to clarify the distinction between the multipoles that newly belong to the identity IR in $P\bar{3}$ and those that originally belong to the identity IR in $P\bar{3}m1$, we henceforth express all multipoles in terms of their irreducible representations under $P\bar{3}m1$. Similarly, the SAMBs are constructed with reference to the $P\bar{3}m1$ system. We confirm that all the A_{2g} multipoles are negligibly small for $\varphi = 0^\circ$, consistent with the $P\bar{3}m1$ symmetry.

Meanwhile, the A_{2g} multipoles take significant values at $\varphi = \pm 16.89^\circ$ under the $P\bar{3}$ symmetry. By comparing the coefficients z_j and the expectation values $\langle\mathbb{Z}_j\rangle$ belonging to the A_{2g} IR at $\varphi = \pm 16.89^\circ$, we can clarify the predominant contributions to the ferroaxial transition. Here, the expectation value $\langle\mathbb{Z}_j\rangle$ is defined as

$$\langle\mathbb{Z}_j\rangle = \frac{1}{N_k}\sum_{n\boldsymbol{k}} f(\varepsilon_{n\boldsymbol{k}}^{\rm SymCW}) \langle n\boldsymbol{k}|\, \mathbb{Z}_j\, |n\boldsymbol{k}\rangle . \tag{7}$$

We find that both z_j and $\langle\mathbb{Z}_j\rangle$ of the ETO $\mathbb{Z}_7^{(G_{3b})}$ in $H_{\rm hop}^{(\rm P-O_{6i},1)}$ have most significant contributions and those of the ETO $\mathbb{Z}_{11}^{(G_{z\alpha})}$ in $H_{\rm hop}^{(\rm Zr-O_{6i},1)}$ also make noticeable contributions. Among the on-site CEF terms, the ETD $\mathbb{Z}_1^{(G_z)}$ in $H_{\rm CEF}^{(\rm O_{6i})}$ and the EH $\mathbb{Z}_3^{(Q_{4b})}$ in $H_{\rm CEF}^{(\rm Zr)}$ exhibit comparatively large coefficients and expectation values. Therefore, we focus on these four terms, $\mathbb{Z}_7^{(G_{3b})}$, $\mathbb{Z}_{11}^{(G_{z\alpha})}$, $\mathbb{Z}_1^{(G_z)}$, and $\mathbb{Z}_3^{(Q_{4b})}$, and present their microscopic definitions and physical interpretations.

Figure 5(a) shows a schematic representation of $\mathbb{Z}_7^{(G_{3b})}$, corresponding to Fig. 3(e). $\mathbb{Z}_7^{(G_{3b})}$ is given by the vortex structure of the spinless atomic E quadrupoles ($Q_v^{\rm (a)}$,

TABLE II: Definitions of SAMBs belonging to the A_{2g} IR of the D_{3d} point group symmetry for $P\bar{3}$ ($\varphi = \pm 16.89°$) and $P\bar{3}m1$ ($\varphi = 0°$) structures. z_j is the coefficient of the SAMB given by Eq. (2) and $\langle \mathbb{Z}_j \rangle$ is the expectation value of the SAMB given by Eq. (7). The symbols $Q^{(\mathrm{a})}$ and $Q^{(\mathrm{s/b})}$ represent the atomic electric and site- or bond-cluster electric bases, respectively. The subscript of $Q^{(\mathrm{a})}$ and $Q^{(\mathrm{s/b})}$ represent the notation of electric bases, which are summarized at References [34, 40]. The column of "Hybridization" represents the corresponding Hilbert space. The rotation angle φ is defined in Fig. 2.

	SAMB	Hybridization	z_j [eV]	$\langle \mathbb{Z}_j \rangle$
			$\varphi = \pm 16.89°$ ($\varphi = 0°$)	$\varphi = \pm 16.89°$ ($\varphi = 0°$)
$H_{\mathrm{CEF}}^{(\mathrm{O_{6i}})}$	$\mathbb{Z}_1^{(G_z)} = \frac{1}{\sqrt{2}} \left(Q_x^{(\mathrm{a,\,E_u})} \otimes Q_y^{(\mathrm{s,\,E_u})} - Q_y^{(\mathrm{a,\,E_u})} \otimes Q_x^{(\mathrm{s,\,E_u})} \right)$	$\langle s,\, \mathrm{O_{6i}} \vert p,\, \mathrm{O_{6i}} \rangle$	$\mp 2.61 \times 10^{-3}$ (-4.68×10^{-12})	$\mp 1.59 \times 10^{-1}$ (-2.45×10^{-14})
	$\mathbb{Z}_2^{(G_{3b})} = \frac{1}{\sqrt{2}} \left(Q_{xy}^{(\mathrm{a,\,E_g})} \otimes Q_{yz}^{(\mathrm{s,\,E_g})} - Q_v^{(\mathrm{a,\,E_g})} \otimes Q_{zx}^{(\mathrm{s,\,E_g})} \right)$	$\langle p,\, \mathrm{O_{6i}} \vert p,\, \mathrm{O_{6i}} \rangle$	$\mp 8.90 \times 10^{-1}$ (3.72×10^{-11})	$\mp 8.11 \times 10^{-2}$ (-5.06×10^{-12})
$H_{\mathrm{CEF}}^{(\mathrm{Zr})}$	$\mathbb{Z}_3^{(Q_{4b})} = Q_{4b}^{(\mathrm{a,\,A_{2g}})} \otimes Q_0^{(\mathrm{s,\,A_{1g}})}$	$\langle d,\, \mathrm{Zr} \vert d,\, \mathrm{Zr} \rangle$	$\pm 3.79 \times 10^{-1}$ (6.01×10^{-11})	$\mp 8.74 \times 10^{-2}$ (-1.72×10^{-12})
$H_{\mathrm{hop}}^{(\mathrm{P-O_{6i}},1)}$	$\mathbb{Z}_4^{(G_z)} = \frac{1}{\sqrt{2}} \left(Q_x^{(\mathrm{a,\,E_u})} \otimes Q_y^{(\mathrm{b,\,E_u})} - Q_y^{(\mathrm{a,\,E_u})} \otimes Q_x^{(\mathrm{b,\,E_u})} \right)$	$\langle p,\, \mathrm{P} \vert s,\, \mathrm{O_{6i}} \rangle$	± 7.10 (-9.73×10^{-11})	$\mp 2.45 \times 10^{-1}$ (5.09×10^{-12})
	$\mathbb{Z}_5^{(G_z)} = \frac{1}{\sqrt{2}} \left(Q_x^{(\mathrm{a,\,E_u})} \otimes Q_y^{(\mathrm{b,\,E_u})} - Q_y^{(\mathrm{a,\,E_u})} \otimes Q_x^{(\mathrm{b,\,E_u})} \right)$	$\langle s,\, \mathrm{P} \vert p,\, \mathrm{O_{6i}} \rangle$	∓ 3.54 (-1.26×10^{-11})	$\pm 1.74 \times 10^{-1}$ (7.41×10^{-12})
	$\mathbb{Z}_6^{(G_z)} = \frac{1}{\sqrt{2}} \left(Q_{zx}^{(\mathrm{a,\,E_g})} \otimes Q_{yz}^{(\mathrm{b,\,E_g})} - Q_{yz}^{(\mathrm{a,\,E_g})} \otimes Q_{zx}^{(\mathrm{b,\,E_g})} \right)$	$\langle p,\, \mathrm{P} \vert p,\, \mathrm{O_{6i}} \rangle$	± 2.86 (1.45×10^{-10})	$\mp 1.73 \times 10^{-1}$ (-1.96×10^{-11})
	$\mathbb{Z}_7^{(G_{3b})} = \frac{1}{\sqrt{2}} \left(Q_{xy}^{(\mathrm{a,\,E_g})} \otimes Q_{yz}^{(\mathrm{b,\,E_g})} - Q_v^{(\mathrm{a,\,E_g})} \otimes Q_{zx}^{(\mathrm{b,\,E_g})} \right)$	$\langle p,\, \mathrm{P} \vert p,\, \mathrm{O_{6i}} \rangle$	± 7.21 (6.02×10^{-12})	$\mp 4.60 \times 10^{-1}$ (-4.26×10^{-13})
$H_{\mathrm{hop}}^{(\mathrm{Zr-O_{6i}},1)}$	$\mathbb{Z}_8^{(G_z)} = \frac{1}{\sqrt{2}} \left(Q_{zx}^{(\mathrm{a,\,E_g})} \otimes Q_{yz}^{(\mathrm{b,\,E_g})} - Q_{yz}^{(\mathrm{a,\,E_g})} \otimes Q_{zx}^{(\mathrm{b,\,E_g})} \right)$	$\langle d,\, \mathrm{Zr} \vert s,\, \mathrm{O_{6i}} \rangle$	± 2.55 (1.29×10^{-10})	$\mp 1.37 \times 10^{-1}$ (-1.69×10^{-12})
	$\mathbb{Z}_9^{(G_{3b})} = \frac{1}{\sqrt{2}} \left(Q_{xy}^{(\mathrm{a,\,E_g})} \otimes Q_{yz}^{(\mathrm{b,\,E_g})} - Q_v^{(\mathrm{a,\,E_g})} \otimes Q_{zx}^{(\mathrm{b,\,E_g})} \right)$	$\langle d,\, \mathrm{Zr} \vert s,\, \mathrm{O_{6i}} \rangle$	± 3.50 (-2.66×10^{-11})	$\mp 1.79 \times 10^{-1}$ (-6.88×10^{-13})
	$\mathbb{Z}_{10}^{(G_{z\alpha})} = \frac{1}{\sqrt{2}} \left(Q_{3u}^{(\mathrm{a,\,E_u})} \otimes Q_y^{(\mathrm{b,\,E_u})} - Q_{3v}^{(\mathrm{a,\,E_u})} \otimes Q_x^{(\mathrm{b,\,E_u})} \right)$	$\langle d,\, \mathrm{Zr} \vert p,\, \mathrm{O_{6i}} \rangle$	$\mp 8.70 \times 10^{-1}$ (-1.41×10^{-12})	$\pm 1.02 \times 10^{-1}$ (-1.47×10^{-12})
	$\mathbb{Z}_{11}^{(G_{z\alpha})} = \frac{1}{2\sqrt{2}} \left(Q_{z\beta}^{(\mathrm{a,\,E_u})} \otimes Q_x^{(\mathrm{b,\,E_u})} - Q_{xyz}^{(\mathrm{a,\,E_u})} \otimes Q_y^{(\mathrm{b,\,E_u})} - \sqrt{6} Q_{3a}^{(\mathrm{a,\,A_{1u}})} \otimes Q_z^{(\mathrm{b,A_{2u}})} \right)$	$\langle d,\, \mathrm{Zr} \vert p,\, \mathrm{O_{6i}} \rangle$	± 4.35 (4.51×10^{-11})	$\mp 3.80 \times 10^{-1}$ (-1.28×10^{-12})
	$\mathbb{Z}_{12}^{(Q_{4b})} = \frac{3}{2\sqrt{6}} \left(Q_{z\beta}^{(\mathrm{a,\,E_u})} \otimes Q_x^{(\mathrm{b,\,E_u})} - Q_{xyz}^{(\mathrm{a,\,E_u})} \otimes Q_y^{(\mathrm{b,\,E_u})} + \frac{2}{\sqrt{6}} Q_{3a}^{(\mathrm{a,\,A_{1u}})} \otimes Q_z^{(\mathrm{b,A_{2u}})} \right)$	$\langle d,\, \mathrm{Zr} \vert p,\, \mathrm{O_{6i}} \rangle$	± 1.67 (-1.56×10^{-10})	$\mp 1.72 \times 10^{-1}$ (1.15×10^{-11})

$Q_{xy}^{(\mathrm{a})}$), which are defined in the (p_x, p_y, p_z) orbitals as

$$Q_{xy}^{(\mathrm{a,\,E_g})} = \frac{\sqrt{2}}{2} \begin{pmatrix} 0 & 1 & 0 \\ 1 & 0 & 0 \\ 0 & 0 & 0 \end{pmatrix}, \quad Q_v^{(\mathrm{a,\,E_g})} = \frac{\sqrt{2}}{2} \begin{pmatrix} 1 & 0 & 0 \\ 0 & -1 & 0 \\ 0 & 0 & 0 \end{pmatrix}. \tag{8}$$

Thus, $\mathbb{Z}_7^{(G_{3b})}$ represents the spin-independent off-diagonal real hopping between p orbitals at nearest-neighbor P and O_{6i} atoms. As shown in Fig. 5(b), for the hopping between P and O_{6i} atoms in the home unit-cell, $\mathbb{Z}_7^{(G_{3b})}$ is given by

$$t_1 (c_{p_y,\mathrm{P}}^{\dagger} c_{p_x,\mathrm{O_{6i}}} + \mathrm{h.c.}), \tag{9}$$

where $c_{p_y,\mathrm{P}}^{\dagger}$ ($c_{p_x,\mathrm{O_{6i}}}$) is the creation (annihilation) operator of the electron with p_y (p_x) orbital at P (O_{6i}) atom in the home unit-cell. Note that the hopping parameter t_1 is related to the coefficient z_7 as $t_1 = z_7/\sqrt{2}$. As shown in Figs. 5(b) and (c), this hopping is allowed only in the fer-

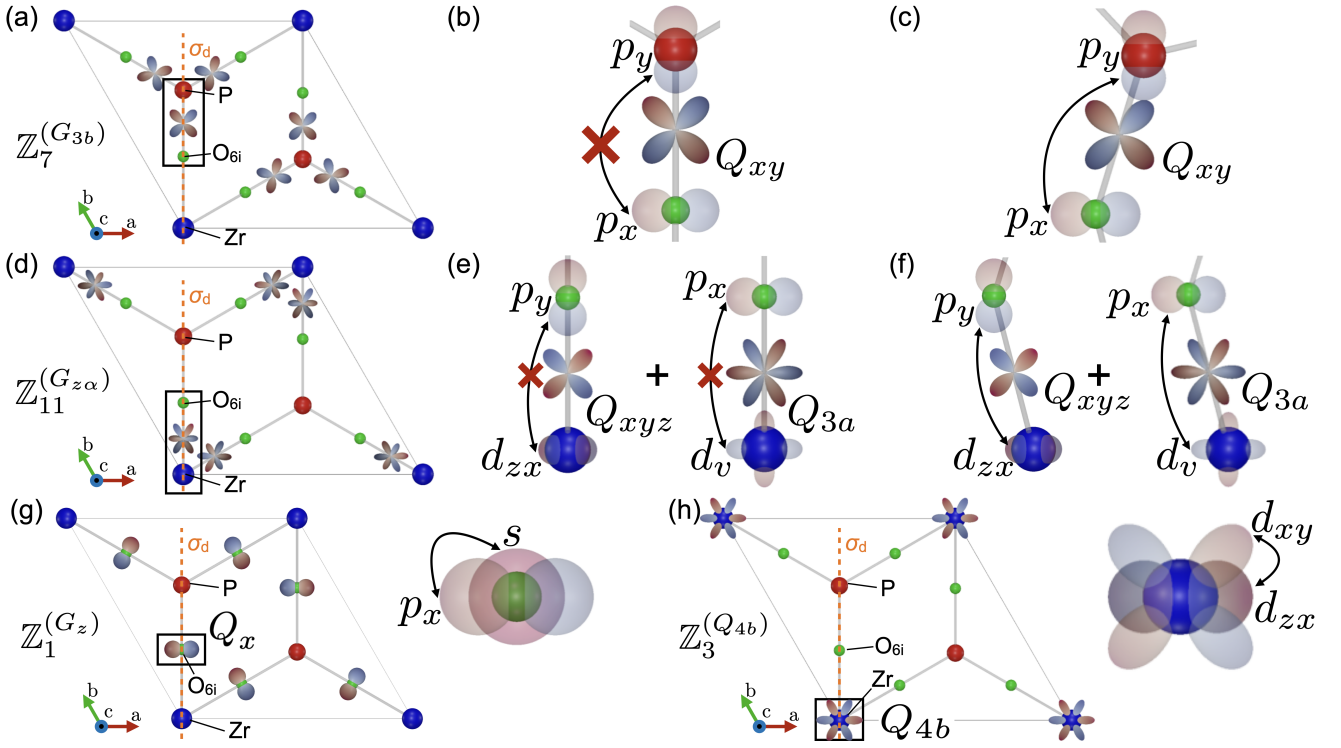

FIG. 5: (a) Schematic representation of $\mathbb{Z}_7^{(G_{3b})}$. (b) Focusing on the region enclosed by the black rectangle in (a), $\mathbb{Z}_7^{(G_{3b})}$ corresponds to the spin-independent off-diagonal real hopping between the p_x orbital at O_{6i} site and the p_y orbital at P site, (c) and this off-diagonal real hopping is allowed in the ferroaxial phase with $\varphi \neq 0$. In the same manner, panels (d), (e), and (f) illustrate the schematic representation of $\mathbb{Z}_{11}^{(G_{z\alpha})}$, corresponding to the spin-independent off-diagonal real hopping between the $p_y(O_{6i})$-$d_{zx}(Zr)$ and $p_x(O_{6i})$-$d_v(Zr)$ orbitals, its hopping prossess at $\varphi = 0$, and that at $\varphi \neq 0$, respectively. Panels (g) and (h) display the representation and the hopping process of $\mathbb{Z}_1^{(G_z)}$ and $\mathbb{Z}_3^{(Q_{4b})}$, respectively.

roaxial phase with $\varphi \neq 0$ by breaking the mirror symmetry σ_d shown in Fig. 2. Indeed, as shown in Table II, z_7 is close to zero when $\varphi = 0°$, while $z_7 = \pm 7.21$ eV in the ferroaxial phase with $\varphi = \pm 16.89°$, and its sign corresponds to the direction of the rotational distortion. Additionally, the expectation value $\langle \mathbb{Z}_7^{(G_{3b})} \rangle$ at $\varphi = \pm 16.89°$ has most significant contribution, $\langle \mathbb{Z}_7^{(G_{3b})} \rangle = \mp 4.60 \times 10^{-1}$.

Similarly, $H_{\rm hop}^{({\rm Zr-O_{6i}},1)}$ contains another ETO $\mathbb{Z}_{11}^{(G_{z\alpha})}$, corresponding to Fig. 3(b). Figure 5(d) shows a schematic representation of $\mathbb{Z}_{11}^{(G_{z\alpha})}$, and the spinless atomic E octupoles ($Q_{z\beta}^{(\rm a)}$, $Q_{xyz}^{(\rm a)}$, $Q_{3a}^{(\rm a)}$) that constitute $\mathbb{Z}_{11}^{(G_{z\alpha})}$ are defined in the p–d hybrid orbitals space $\langle p|d\rangle$ as

$$Q_{z\beta}^{(\rm a,\,E_u)} = \frac{\sqrt{3}}{3}\begin{pmatrix} 0 & 0 & 0 & -1 & 0 \\ 0 & 0 & 1 & 0 & 0 \\ 0 & -1 & 0 & 0 & 0 \end{pmatrix}, \tag{10}$$

$$Q_{xyz}^{(\rm a,\,E_u)} = \frac{\sqrt{3}}{3}\begin{pmatrix} 0 & 0 & 1 & 0 & 0 \\ 0 & 0 & 0 & 1 & 0 \\ 0 & 0 & 0 & 0 & 1 \end{pmatrix}, \tag{11}$$

$$Q_{3a}^{(\rm a,\,A_{1u})} = \frac{\sqrt{2}}{2}\begin{pmatrix} 0 & 1 & 0 & 0 & 0 \\ 0 & 0 & 0 & 0 & -1 \\ 0 & 0 & 0 & 0 & 0 \end{pmatrix}, \tag{12}$$

where the rows and columns correspond to the (p_x, p_y, p_z) orbitals and the $(d_u, d_v, d_{yz}, d_{zx}, d_{xy})$ orbitals with $v = x^2 - y^2$, respectively. Accordingly, $\mathbb{Z}_{11}^{(G_{z\alpha})}$ represents the spin-independent off-diagonal real hopping between d orbitals on Zr atoms and p orbitals on O_{6i} atoms. As shown in Fig. 5(e), for the hopping between Zr and O_{6i} atoms in the home unit-cell, $\mathbb{Z}_{11}^{(G_{z\alpha})}$ is given by

$$t_2(c^\dagger_{d_{zx},{\rm Zr}} c_{p_y,{\rm O_{6i}}} + {\rm h.c.}) + t_3(c^\dagger_{d_v,{\rm Zr}} c_{p_x,{\rm O_{6i}}} + {\rm h.c.}), \tag{13}$$

where $c^\dagger_{d_v,{\rm Zr}}$ ($c_{p_y,{\rm O_{6i}}}$) is the creation (annihilation) operator of the electron with d_v (p_y) orbital at Zr (O_{6i}) atom

in the home unit-cell. The hopping parameters t_2 and t_3 are related to the coefficient z_{11} as $t_2 = z_{11}/6\sqrt{2}$ and $t_3 = z_{11}/4$, respectively. Similarly to $\mathbb{Z}_7^{(G_{3b})}$, this hopping is allowed only in the ferroaxial phase with $\varphi \neq 0°$ by breaking the mirror symmetry $\sigma_{\rm d}$, as shown in Figs. 5(e) and (f). This is confirmed from the DFT calculations, where z_{11} is close to zero when $\varphi = 0°$, while $z_{11} = \pm 4.35$ eV in the ferroaxial phase with nonzero φ, and its sign is reversed according to the direction of the rotational distortion, as shown in Table II. The expectation value $\mathbb{Z}_{11}^{(G_{z\alpha})}$ at $\varphi = \pm 16.89°$ is the second largest following $\langle \mathbb{Z}_7^{(G_{3b})} \rangle$, $\langle \mathbb{Z}_{11}^{(G_{z\alpha})} \rangle = \mp 3.80 \times 10^{-1}$.

In the CEF terms, the ETD $\mathbb{Z}_1^{(G_z)}$ in $H_{\rm CEF}^{(\rm O_{6i})}$ and the EH $\mathbb{Z}_3^{(Q_{4b})}$ in $H_{\rm CEF}^{(\rm Zr)}$ also make noticeable contributions. As shown in Fig. 5(g), the site-cluster ETD $\mathbb{Z}_1^{(G_z)}$ arises from the vortex-like configuration of the spinless atomic E dipoles $\boldsymbol{Q}^{(\rm a)} = (Q_x^{(\rm a)}, Q_y^{(\rm a)})$ on the O_{6i} atoms, which are defined in $\langle s|p\rangle$ orbitals space as

$$Q_x^{(\rm a,\,E_u)} = \begin{pmatrix} 1 & 0 & 0 \end{pmatrix}, \quad Q_y^{(\rm a,\,E_u)} = \begin{pmatrix} 0 & 1 & 0 \end{pmatrix}. \tag{14}$$

This ETD is also allowed only in the ferroaxial phase with $\varphi \neq 0$, leading to the on-site hybridization between the s and (p_x, p_y) orbitals at the O_{6i} sites. On the other hand, $\mathbb{Z}_3^{(Q_{4b})}$ corresponds to the atomic EH $Q_{4b}^{(\rm a)}$ on the Zr atom, which are defined in the (d_u, d_v, d_{xy}, d_{yz}, d_{zx}) orbitals:

$$Q_{4b}^{(\rm a,\,A_{2g})} = \frac{1}{2}\begin{pmatrix} 0 & 0 & 0 & 0 & 0 \\ 0 & 0 & 0 & -1 & 0 \\ 0 & 0 & 0 & 0 & 1 \\ 0 & -1 & 0 & 0 & 0 \\ 0 & 0 & 1 & 0 & 0 \end{pmatrix}. \tag{15}$$

As shown in Fig. 5(h), $\mathbb{Z}_3^{(Q_{4b})}$ corresponds to the d_v-d_{yz} and d_{zx}-d_{xy} hybridization between the d orbitals at the Zr atom. The signs of the coefficients z_1 and z_3, as well as those of the expectation values $\langle \mathbb{Z}_1^{(G_z)} \rangle$ and $\langle \mathbb{Z}_3^{(Q_{4b})} \rangle$, correspond to the direction of the rotational distortion.

From the above results, we conclude that the two ETOs $\mathbb{Z}_7^{(G_{3b})}$, corresponding to the spin-independent off-diagonal real hopping between p orbitals at nearest-neighbor P and O_{6i} atoms, and $\mathbb{Z}_{11}^{(G_{z\alpha})}$, corresponding to the spin-independent off-diagonal real hopping between d orbitals on Zr atoms and p orbitals on O_{6i} atoms, provide the dominant contributions to the ferroaxial transition. In addition, the ETD $\mathbb{Z}_1^{(G_z)}$ in $H_{\rm CEF}^{(\rm O_{6i})}$ and the EH $\mathbb{Z}_3^{(Q_{4b})}$ in $H_{\rm CEF}^{(\rm Zr)}$, have also significant contribution to the CEF terms in the ferroaxial phase.

To further clarify the orbital characters involved in the relevant hybridizations associated with the above four multipoles, we evaluate the energy-resolved expectation values $\langle \mathbb{Z}_j \rangle (E)$ for $\varphi = \pm 16.89°$, which is defined as

$$\langle \mathbb{Z}_j \rangle (E) = \frac{1}{N_k} \sum_{n\boldsymbol{k}} \langle n\boldsymbol{k}| \mathbb{Z}_j |n\boldsymbol{k}\rangle \, \delta(\varepsilon_{n\boldsymbol{k}} - E). \tag{16}$$

Figure 6 shows the energy-resolved expectation values, $\langle \mathbb{Z}_7^{(G_{3b})} \rangle (E)$, $\langle \mathbb{Z}_{11}^{(G_{z\alpha})} \rangle (E)$, $\langle \mathbb{Z}_1^{(G_z)} \rangle (E)$, and $\langle \mathbb{Z}_3^{(Q_{4b})} \rangle (E)$ together with the DOS in Fig. 4(a). They take nonzero values in the ferroaxial phase, and their signs reverse according to the direction of the rotational distortion, indicating that these multipoles serve as quantitative measures of the ferroaxiality. Notably, the bond-cluster ETOs $\langle \mathbb{Z}_7^{(G_{3b})} \rangle (E)$ and $\langle \mathbb{Z}_{11}^{(G_{z\alpha})} \rangle (E)$ show opposite signs in the valence and conduction bands, being positive in the valence bands and negative in the conduction bands. In contrast, the site-cluster ETD $\langle \mathbb{Z}_1^{(G_z)} \rangle (E)$ and the atomic EH $\langle \mathbb{Z}_3^{(Q_{4b})} \rangle (E)$ exhibit oscillatory behavior with both positive and negative values across the valence and conduction bands.

Furthermore, each peak appearing in $\langle \mathbb{Z}_j \rangle (E)$ corresponds to a peak in the DOS of the relevant orbitals involved in the hybridization associated with $\mathbb{Z}_j$. Once the ferroaxial order appears, additional off-diagonal hybridizations among the p–p, s–p, and p–d orbitals emerge. These hybridizations induce new bonding and antibonding states, giving rise to additional peaks in the DOS that are absent in the nonferroaxial phase.

B. Rotation angle dependence of ferroaxiality

We show the evolution of the expectation values $\langle \mathbb{Z}_j \rangle$ of the four SAMBs by systematically changing the rotation angle φ from 0° to ±30°, while keeping the lattice constants and the $\rm P - O_{6i}$ bond length fixed at the values obtained from the structural optimization. Note that the $\rm Zr - O_{6i}$ bond length varies with φ. Figure 7 presents how $\langle \mathbb{Z}_j \rangle$, which characterize the strength of the multipoles in the electronic states, evolves with the rotation angle φ. As shown in Figs. 7(b), (d), (f), and (h), $\langle \mathbb{Z}_j \rangle$ vanishes in the nonferroaxial phase with the mirror symmetry $\sigma_{\rm d}$ ($\varphi = 0°$), whereas it becomes finite in the ferroaxial phase ($\varphi \neq 0°$) and increases linearly with increase of φ from zero. Furthermore, The sign of $\langle \mathbb{Z}_j \rangle$ reverses depending on the direction of rotation. Therefore, $\langle \mathbb{Z}_7^{(G_{3b})} \rangle$, $\langle \mathbb{Z}_{11}^{(G_{z\alpha})} \rangle$, $\langle \mathbb{Z}_1^{(G_z)} \rangle$, and $\langle \mathbb{Z}_3^{(Q_{4b})} \rangle$ play as proper indicators of ferroaxiality, and their sign correspond to the direction of rotation.

C. Effect of relativistic spin-orbit coupling

Finally, we discuss the effect of the relativistic SOC on the ferroaxial transition, especially the contribution of the spinful ETD represented by the cross-product–type SOC $G_z' = (\boldsymbol{l} \times \boldsymbol{\sigma})_z/\sqrt{2}$ [34], where $\boldsymbol{l}$ and $\boldsymbol{\sigma}$ denote the atomic orbital and spin angular momenta, respectively. We also performed DFT calculation by using the fully-relativistic ONCV pseudopotentials [47] downloaded from PseudoDojo [48] at $\varphi = \pm 16.89°$, and built spinful SymCW models. All the parameters used in the DFT calculation keeps as same as the spinless calcula-

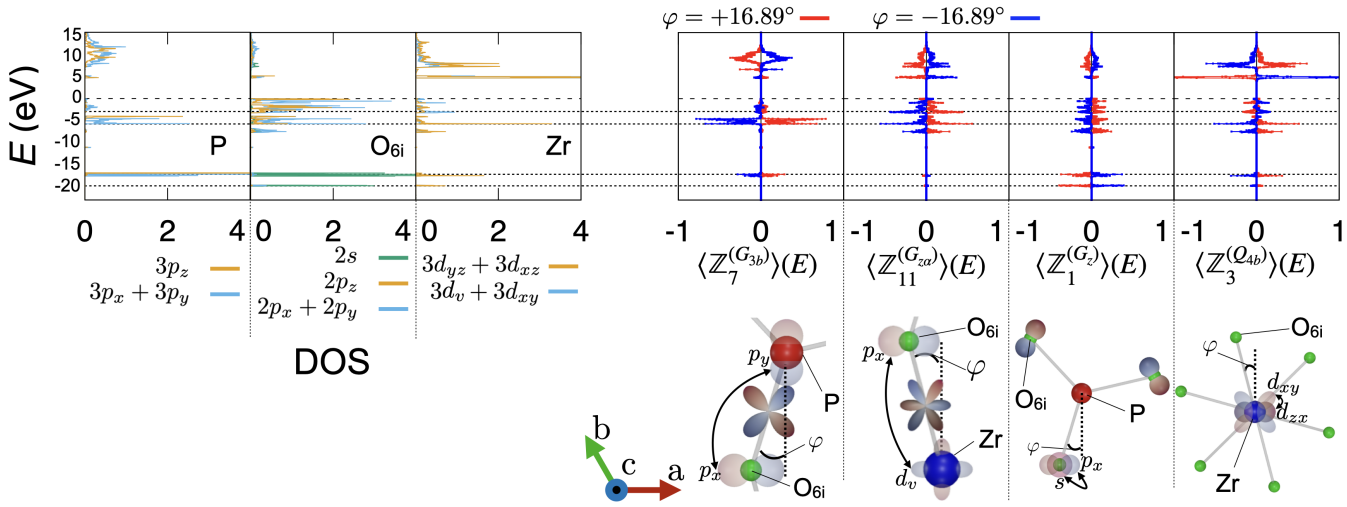

FIG. 6: Energy-resolved expectation values $\langle \mathbb{Z}_j \rangle(E)$ given by Eq. (16) (right panel) together with the DOS (left panel) obtained from the DFT calculations in Fig. 4(b). The red and blue lines represent the results for $\varphi = +16.89°$ and $\varphi = -16.89°$, respectively. Please extend the energy-range as [-23 eV,15 eV].

TABLE III: Coefficient z'_j and expectation value $\langle \mathbb{Z}'_j \rangle$ of the site-cluster spinful ETD G'_z at P, Zr, and O_{6i} atoms. The column of "Hybridization" represents the corresponding Hilbert space.

Hybridization	$z_j'^{(G_z)}$ [eV]	$\langle \mathbb{Z}'_j \rangle$
$\langle p, \mathrm{P} \vert p, \mathrm{P} \rangle$	9.33×10^{-5}	1.88×10^{-4}
$\langle d, \mathrm{Zr} \vert d, \mathrm{Zr} \rangle$	-1.05×10^{-3}	1.65×10^{-6}
$\langle p, \mathrm{O_{6i}} \vert p, \mathrm{O_{6i}} \rangle$	-1.14×10^{-2}	1.06×10^{-3}

tion with the scalar-relativistic ONCV pseudopotentials. By considering the SOC, the additional SOC-driven local term H_{SOC} is appeared in the SymCW Hamiltonian given by Eq. (4), and it is expressed as the linear combination of the product of the spinful SAMB $\mathbb{Z}'_j$ and its coefficient z'_j, where the prime denotes the spinful term. Using the obtained spinful SymCW models, we evaluated the coefficient z'_j and the expectation value $\langle \mathbb{Z}'_j \rangle$ of the spinful ETD G'_z at P, Zr, O_{6i} atoms, which are summarized in Table. III.

As shown in Table. III, the contributions of the spinful ETDs are orders of magnitude smaller than those of the spinless ferroaxial terms located at the same atom in Table. II. We further examined the other spinful contributions including spin-dependent hoppings, and confirmed that their magnitudes are below 4×10^{-2} and 2×10^{-3} for z'_j and $\langle \mathbb{Z}'_j \rangle$, respectively. In addition, we confirmed that the coefficients of the spinless ferroaxial SAMBs, such as z_7, z_{11}, z_1 and z_3, and the corresponding expectation values, $\langle \mathbb{Z}_7^{(G_{3b})} \rangle$, $\langle \mathbb{Z}_{11}^{(G_{z\alpha})} \rangle$, $\langle \mathbb{Z}_1^{(G_z)} \rangle$ and $\langle \mathbb{Z}_3^{(Q_{4b})} \rangle$ are quantitatively almost unchanged as shown in Table. IV.

Therefore, we conclude that the relativistic SOC has a negligible influence on the ferroaxial transition.

TABLE IV: Coefficient z_j and expectation value $\langle \mathbb{Z}_j \rangle$ of $\mathbb{Z}_7^{(G_{3b})}$, $\mathbb{Z}_{11}^{(G_{z\alpha})}$, $\mathbb{Z}_1^{(G_z)}$ and $\mathbb{Z}_3^{(Q_{4b})}$ calculated with SOC and without SOC at $\varphi = 16.89°$.

SAMB	z_j [eV] (w/o SOC)	$\langle \mathbb{Z}_j \rangle$ (w/o SOC)
$\mathbb{Z}_7^{(G_{3b})}$	4.05 (7.21)	-2.44×10^{-1} (-4.60×10^{-1})
$\mathbb{Z}_{11}^{(G_{z\alpha})}$	6.16 (4.35)	-5.38×10^{-1} (-3.80×10^{-1})
$\mathbb{Z}_1^{(G_z)}$	-1.14×10^{-3} (-2.61×10^{-3})	-2.24×10^{-1} (-1.59×10^{-1})
$\mathbb{Z}_3^{(Q_{4b})}$	5.36×10^{-1} (3.79×10^{-1})	-1.24×10^{-1} (-8.74×10^{-2})

VI. CONCLUSION

We have performed a comprehensive microscopic analysis of the displacive-type ferroaxial transition in $K_2Zr(PO_4)_2$ by combining DFT calculations with a SymCW approach formulated in the framework of SAMB. This method has enabled us to quantify the electronic ferroaxial degrees of freedom directly from realistic band structures and to decompose the Hamiltonian into a linear combination of the complete set of spinless multipoles. Within this multipole-based description, we have identified that the ETD, ETO, and EH, all sharing the same symmetry, emerge as the key microscopic ingredients of the ferroaxial phase. Among them, the bond-cluster ETOs associated with the P-O_{6i} and Zr-O_{6i} bonds provide the dominant contributions: they arise from spin-independent off-diagonal real hoppings between the p orbitals on P and O atoms and between the d orbitals on Zr atoms and the p orbitals on O atoms. We have further shown that the site-cluster ETD at the O_{6i} sites and the

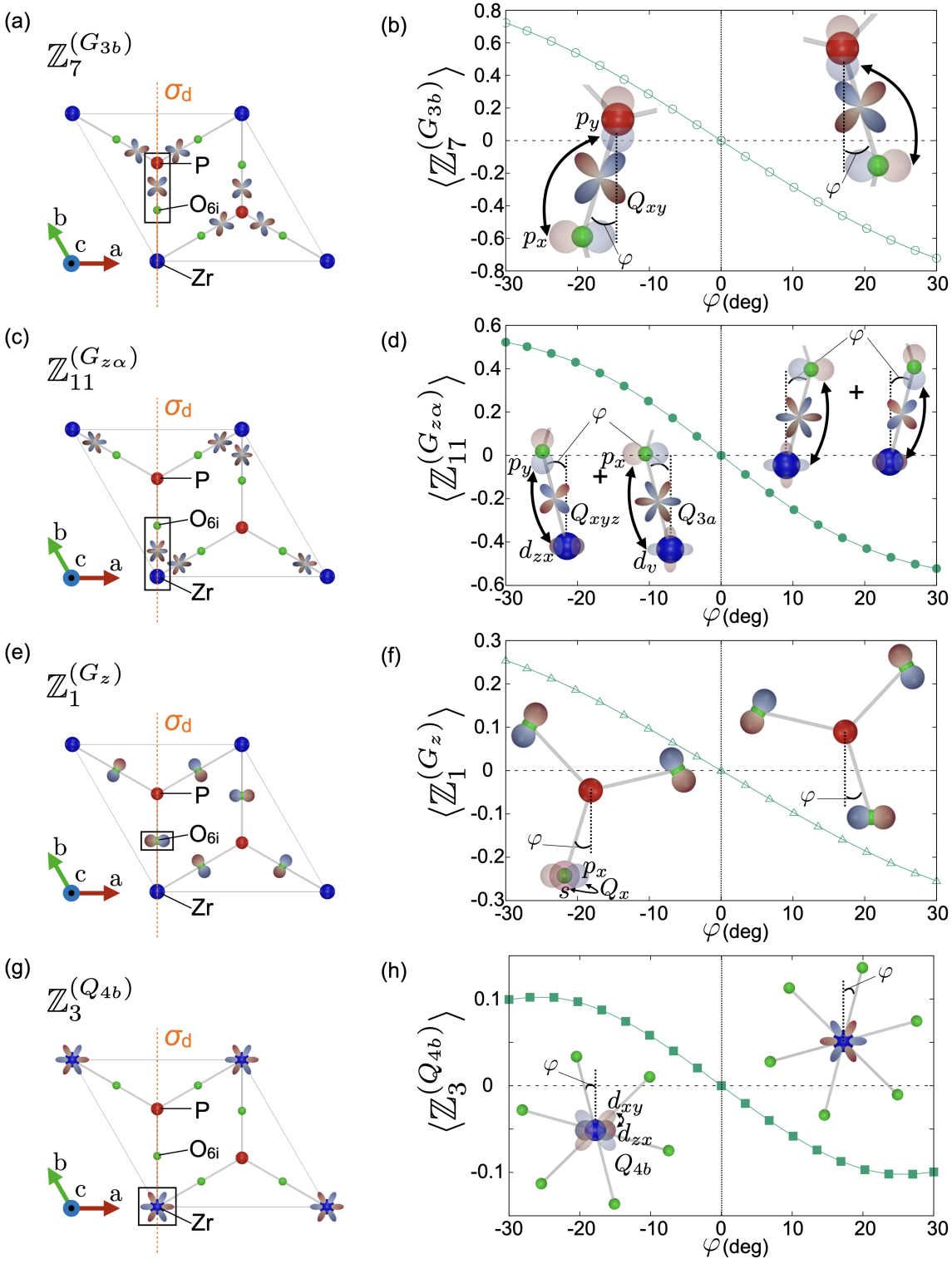

FIG. 7: SAMBs belonging to the A_{2g} IR are shown in the left column: those located at (a) the P−O$_{6i}$ bond ($\mathbb{Z}_7^{(G_{3b})}$), (c) the Zr−O$_{6i}$ bond ($\mathbb{Z}_{11}^{(G_{z\alpha})}$), (e) the O$_{6i}$ site ($\mathbb{Z}_1^{(G_z)}$), and (g) the Zr site ($\mathbb{Z}_3^{(Q_{4b})}$). The mirror symmetry σ_d, indicated by the orange dashed line, forbids these hybridizations at $\varphi = 0°$. When the symmetry is reduced to $P\bar{3}$, σ_d is broken, and the SAMBs become nonzero, as shown in the right column. The variations in the expectation values of the SAMBs respect to φ are also shown in the right column.

atomic EH at the Zr sites also make non-negligible contributions through on-site hybridizations between s and (p_x, p_y) orbitals and between different d orbitals, respectively. The expectation values of these multipoles vanish in the nonferroaxial $P\bar{3}m1$ phase, while those become finite in the ferroaxial $P\bar{3}$ phase, and grow approximately linearly with the rotation angle φ, with their signs following the direction of the rotational distortion. They therefore serve as quantitative order parameters for the electronic aspect of ferroaxiality. Furthermore, we have demonstrated that the effect of relativistic SOC is negligibly small in the ferroaxial transition.

Overall, our results demonstrate that the essential electronic-origin ferroaxiality in $K_2Zr(PO_4)_2$ arises predominantly from spin-independent orbital hybridizations among different orbitals and different atoms, rather than from relativistic SOC. The present analysis highlights the power of the SAMB-based SymCW framework for disentangling microscopic ferroaxial degrees of freedom in real materials, and it provides a useful basis for exploring ferroaxiality and related rotational structural transitions in a broader class of compounds.

ACKNOWLEDGMENTS

The authors thank H. Kusunose for fruitful discussions. This work was supported by JSPS KAKENHI Grants Numbers JP22H00101, JP22H01183, JP23H04869, JP23K03288, and by JST CREST (JPMJCR23O4) and JST FOREST (JPMJFR2366).

[1] W. Jin, E. Drueke, S. Li, A. Admasu, R. Owen, M. Day, K. Sun, S.-W. Cheong, and L. Zhao, Nat. Phys. **16**, 42 (2020).
[2] J. Hlinka, Phys. Rev. Lett. **113**, 165502 (2014).
[3] J. Hlinka, J. Privratska, P. Ondrejkovic, and V. Janovec, Phys. Rev. Lett. **116**, 177602 (2016).
[4] R. Owen, E. Drueke, C. Albunio, A. Kaczmarek, W. Jin, D. Obeysekera, S.-W. Cheong, J. Yang, S. Cundiff, and L. Zhao, Phys. Rev. B **103**, 054104 (2021).
[5] X. Guo, R. Owen, A. Kaczmarek, X. Fang, C. De, Y. Ahn, W. Hu, N. Agarwal, S. H. Sung, R. Hovden, S.-W. Cheong, and L. Zhao, Phys. Rev. B **107**, L180102 (2023).
[6] Z. Zeng, M. Först, M. Fechner, D. Prabhakaran, P. Radaelli, and A. Cavalleri, Science **390**, 195 (2025).
[7] T. Hayashida, Y. Uemura, K. Kimura, S. Matsuoka, D. Morikawa, S. Hirose, K. Tsuda, T. Hasegawa, and T. Kimura, Nat. Commun. **11**, 4582 (2020).
[8] T. Hayashida, Y. Uemura, K. Kimura, S. Matsuoka, M. Hagihala, S. Hirose, H. Morioka, T. Hasegawa, and T. Kimura, Phys. Rev. Materials **5**, 124409 (2021).
[9] H. Yokota, T. Hayashida, D. Kitahara, and T. Kimura, npj Quantum Mater. **7**, 106 (2022).
[10] X. Fang, C. De, F.-T. Huang, X. Xu, K. Du, K. Wang, B. Li, and S.-W. Cheong, J. Am. Chem. Soc. **145**, 28022 (2023).
[11] T. Hasegawa, W. Yoshida, K. Nakamura, N. Ogita, and K. Matsuhira, J. Phys. Soc. Jpn. **89**, 054602 (2020).
[12] H. Hanate, T. Hasegawa, S. Hayami, S. Tsutsui, S. Kawano, and K. Matsuhira, J. Phys. Soc. Jpn. **90**, 063702 (2021).
[13] H. Hanate, S. Tsutsui, T. Yajima, H. Nakao, H. Sagayama, T. Hasegawa, and K. Matsuhira, J. Phys. Soc. Jpn. **92**, 063601 (2023).
[14] S. Hayami, S. Tsutsui, H. Hanate, N. Nagasawa, Y. Yoda, and K. Matsuhira, J. Phys. Soc. Jpn. **92**, 033702 (2023).
[15] X. Xu, F.-T. Huang, A. S. Admasu, M. Kratochvílová, M.-W. Chu, J.-G. Park, and S.-W. Cheong, Phys. Rev. B **105**, 184407 (2022).
[16] T. Nagai and T. Kimura, Chem. Mater. **35**, 4109 (2023).
[17] T. Nagai, Y. Mochizuki, S. Yoshida, and T. Kimura, J. Am. Chem. Soc. **145**, 8090 (2023).
[18] D. Sekine, T. Sato, Y. Tokunaga, T.-h. Arima, and M. Matsubara, Phys. Rev. Mater. **8**, 064406 (2024).
[19] B. Singh, G. McNamara, K.-M. Kim, S. Siddique, S. D. Funni, W. Zhang, X. Luo, P. Sakrikar, E. M. Kenney, R. Singha, *et al.*, Nat. Phys. **21**, 1578 (2025).
[20] J. Nasu and S. Hayami, Phys. Rev. B **105**, 245125 (2022).
[21] A. Roy, M. H. D. Guimarães, and J. Sławińska, Phys. Rev. Materials **6**, 045004 (2022).
[22] S. Hayami, R. Oiwa, and H. Kusunose, J. Phys. Soc. Jpn. **91**, 113702 (2022).
[23] A. Inda and S. Hayami, J. Phys. Soc. Jpn. **92**, 043701 (2023).
[24] K. Du, D. Jo, X. Xu, F.-T. Huang, M.-H. Lee, M.-W. Chu, K. Wang, D. Vanderbilt, H.-W. Lee, and S.-W. Cheong, arXiv:2510.00462 (2025).
[25] S.-W. Cheong, S. Lim, K. Du, and F.-T. Huang, npj Quantum Mater. **6**, 58 (2021).
[26] S.-W. Cheong, F.-T. Huang, and M. Kim, Rep. Prog. Phys. **85**, 124501 (2022).
[27] S. Hayami and H. Kusunose, J. Phys. Soc. Jpn. **92**, 113704 (2023).
[28] V. A. Martinez, Y. Gao, J. Yang, F. Lyzwa, Z. Liu, C. J. Won, K. Du, V. Kiryukhin, S. W. Cheong, and A. A. Sirenko, Phys. Rev. B **112**, 064411 (2025).
[29] S. Hayami, R. Oiwa, and A. Inda, J. Phys. Soc. Jpn. **94**, 123702 (2025).
[30] A. Inda and S. Hayami, Phys. Rev. B **111**, L041104 (2025).
[31] S. Bhowal and N. A. Spaldin, Phys. Rev. Res. **6**, 043141 (2024).
[32] V. Dubovik and A. Cheshkov, Sov. J. Part. Nucl **5**, 318 (1975).
[33] V. Dubovik, L. Tosunyan, and V. Tugushev, Zh. Eksp. Teor. Fiz **90**, 590 (1986).
[34] S. Hayami, M. Yatsushiro, Y. Yanagi, and H. Kusunose, Phys. Rev. B **98**, 165110 (2018).
[35] R. Oiwa and H. Kusunose, Phys. Rev. Res. **7**, 033250 (2025).
[36] T. Ishitobi and K. Hattori, arXiv:2502.13977 (2025).
[37] S. Yamagishi, T. Hayashida, R. Misawa, K. Kimura, M. Hagihala, T. Murata, S. Hirose, and T. Kimura, Chem. Mater. **35**, 747 (2023).

[38] T. Ozaki, Phys. Rev. B **110**, 125115 (2024).
[39] R. Oiwa, A. Inda, S. Hayami, T. Nomoto, R. Arita, and H. Kusunose, Phys. Rev. B **112**, 035116 (2025).
[40] H. Kusunose, R. Oiwa, and S. Hayami, Phys. Rev. B **107**, 195118 (2023).
[41] H. Kusunose and S. Hayami, J. Phys.: Condens. Matter **34**, 464002 (2022).
[42] S. Hayami and H. Kusunose, J. Phys. Soc. Jpn. **93**, 072001 (2024).
[43] H. Kusunose, R. Oiwa, and S. Hayami, J. Phys. Soc. Jpn. **89**, 104704 (2020).
[44] M.-T. Suzuki, T. Koretsune, M. Ochi, and R. Arita, Phys. Rev. B **95**, 094406 (2017).
[45] S. Hayami, Y. Yanagi, H. Kusunose, and Y. Motome, Phys. Rev. Lett. **122**, 147602 (2019).
[46] P. Giannozzi, S. Baroni, N. Bonini, M. Calandra, R. Car, C. Cavazzoni, D. Ceresoli, G. L. Chiarotti, M. Cococcioni, I. Dabo, A. Dal Corso, S. de Gironcoli, S. Fabris, G. Fratesi, R. Gebauer, U. Gerstmann, C. Gougoussis, A. Kokalj, M. Lazzeri, L. Martin-Samos, N. Marzari, F. Mauri, R. Mazzarello, S. Paolini, A. Pasquarello, L. Paulatto, C. Sbraccia, S. Scandolo, G. Sclauzero, A. P. Seitsonen, A. Smogunov, P. Umari, and R. M. Wentzcovitch, Journal of Physics: Condensed Matter **21**, 395502 (2009).
[47] D. R. Hamann, Phys. Rev. B **88**, 085117 (2013).
[48] M. van Setten, M. Giantomassi, E. Bousquet, M. Verstraete, D. Hamann, X. Gonze, and G.-M. Rignanese, Computer Physics Communications **226**, 39 (2018).